Aerodynamic Analysis of Rotor Airfoils with Camber Morphing Mechanism versus Plain Flaps

Amine Abdelmoula* Fabian Grimm† Ilkay Yavrucuk ‡

Institute of Helicopter Technology and VTOL,
Technical University of Munich, 80333 Munich, Germany

Jürgen Rauleder §
Daniel Guggenheim School of Aerospace Engineering,
Georgia Institute of Technology, Atlanta, GA 30332, USA

This study presents a comprehensive comparison between standard plain flap configurations and the FishBAC parabolic morphed camber concept. NACA23012 and SC1094R8 airfoils served as baseline configurations. Numerical simulations were performed with a free stream Mach number of $M = 0.4$ and angles of attack of $\alpha = [-5, \alpha_{stall}]$. By analyzing deflection levels up to 4 percent of the chord and varying the starting point of camber morphing from 60% to 85% chord length, key aerodynamic parameters such as lift, lift-to-drag ratio, pitching moment, and center of pressure were evaluated. Both FishBAC and plain flap configurations showed significant lift improvements with increasing deflection levels, particularly in the case of FishBAC camber morphed airfoils and when camber morphing was shifted towards the trailing edge. Furthermore, the overall FishBAC configurations exhibited greater efficiency compared to the plain flap. As camber morphing was increased, the center of pressure shifted towards the trailing edge. The position of the center of pressure exhibited a remarkable sensitivity to the point at which the camber morphing started when the plain flap was applied. Higher deflections resulted in pronounced nose-down pitching moments compared to the baseline, which was most pronounced for the FishBAC camber morphed airfoils.

1 INTRODUCTION

In order to improve the aerodynamic efficiency of a helicopter, more specifically of the main rotor, either static or dynamic modifications to the blade sections may be considered. The implementation of rotors featuring different airfoils on certain radial sections would be an example of static rotor design enhancement. E.g., the main rotor of the U.S. utility class helicopter UH-60A Black Hawk consists of four blades, each with the SC1094 R8 airfoil covering the 48–84$\%R$ section while the SC1095 airfoil is used for the remainder of the span [1]. The ability to dynamically change the shape of an airfoil during operation could facilitate further improvements in performance and efficiency across a wider spectrum of flow conditions [2]. In comparison to the static approach, this would however increase the mechanical complexity within each blade, thus raising the cost of development and production. A variety of shape parameters could be used as the basis for dynamic actuation. One of those is the camber, which has a major influence on an airfoil's aerodynamic characteristics. A number of active camber concepts have been developed so far, the most prevalent one being the plain flap. This approach provides a mechanically simple way of increasing the airfoil's camber, thus improving its maximum lift capability. However this improvement in lift is accompanied by increased drag, caused by the abrupt bend on the airfoil surface and the resulting large pressure gradients near the hinge [3]. In the last decade, new active camber concepts were investigated, where the camber line of the airfoil was morphed following a continuous parabolic deflection so that a smoothed airfoil shape is obtained. Recently, Hunsaker et al. [4] investigated such a camber morphing concept on a fixed-wing airfoils and showed that applying a continuous parabolic deflection to the airfoil profile can reduce drag significantly compared to a plain flap. This reduction was found to be up to 50% for high flap-chord fractions. Woods and Friswell

* Doctoral Candidate, amine.abdelmoula@tum.de
† Graduate Student, f.grimm@tum.de
‡ Professor, ilkay.yavrucuk@tum.de
§ Assistant Professor, juergen.rauleder@gatech.edu

proposed in [3] other alternative mechanism to traditional trailing-edge flaps to introduce a camber change, called the Fish Bone Active Camber (FishBAC) concept and showed in [5] that applying the FishBAC to a symmetric baseline airfoil NACA0012 improved the aerodynamic efficiency by up to 25% in a comparison to a traditional (but sealed) trailing-edge flap. The investigations published by Hunsaker et al. and Woods al. showed that parabolic morphing of the camber has a significant to improve the lift-to-drag ratio of a baseline airfoil. This potential can improve the overall rotor lift-to-drag ratio and thus the required power of the rotor while the camber of a baseline section is dynamically morphed as showed by Rauleder et al. [2] and Dominik et al. in [6–8].

The main purpose of the present paper is to provide further insight into the aerodynamic effects of the aforementioned FishBAC concept by examining the static aerodynamic performance and comparing it to a corresponding plain flap mechanism for different rotor airfoils. Although the flow conditions of a helicopter rotor are highly unsteady and three-dimensional, the rotor performance can be approximated by means of the static and two-dimensional airfoil characteristics [1, 9]. For the proposed paper, a numerical CFD analysis has been conducted on FishBAC and plain flap variants of the airfoils NACA23012 and SC1094R8, considering beginnings of camber morphing ranging from 60–85 %c. In order to obtain a more accurate geometrical representation of a physical FishBAC morphing mechanism compared to past research, a transformation of baseline coordinates was developed, which maintains the camber line length as well as the original thickness distribution. The results of 2D airfoil performance analyses may also be used for the improvement of comprehensive analytical models by contributing the aerodynamic characteristics of the main rotor blade sections [10].

2 METHODOLOGY

In this study a generic tool was developed to facilitate the generation of camber-morphed helicopter airfoil shapes based on specified requirements, along with the automation of 2D CFD grid generation. The tool takes in several input parameters, including a normalized point cloud representing a baseline airfoil, the starting point for camber morphing, the desired airfoil deflection specified as a percentage of chord length, the free stream Mach number, ambient temperature, and the desired y^+ value for CFD grid near the wall, and the chord length of the baseline airfoil.

Figure 1 summarizes the relevant steps executed to generate the shape of the morphed airfoil. The provided

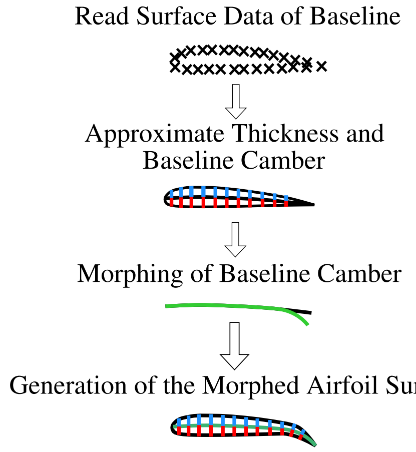

Fig. 1: Summary of the relevant steps to generate the morphed airfoils

baseline, represented as a point cloud, was smoothed using Bezier splines to achieve finely-resolved airfoil shapes. This transformation ensures a refined spatial discretization on the surface, in order to capture the surface curvature of the airfoil. This process serves to eliminate significant roughness in surface gradients, leading to a more well-resolved geometric representation of the airfoil under investigation. To approximate the airfoil's camber line, the thickness distribution is computed by approximating the vertical distance between the upper and lower surfaces. This computation involves the discretization of both the upper and lower surfaces along the same set of x coordinates. Subsequently, the baseline camber is determined as the line passing through the midpoint of the computed thickness t. This comprehensive approach ensures a thorough and dependable depiction of the intricate airfoil shape.

The concept of generating a parabolic morphed camber was inspired by the FishBAC concept, which was introduced by Woods et al. [11].

Figure 2 illustrates how the parabolic camber is applied the baseline along the morphing section defined between x_r and x_t.

For values of x_b in the range $[x_t, 1]$, the trailing edge of the baseline is assumed to be rigid. The process of determining the coordinates x_{m_i} and y_{m_i} along the morphed camber involved discretizing the interval $[x_r, x_t]$ and defining x_{m_i} and y_{m_i} as follows:

$$x_{m_i} = x_{m_{i-1}} + (x_{b i} - x_{b i-1}) \cos(\theta_{i-1}) \tag{1}$$

$$y_{m_i} = y_{b_i} + \tilde{y}_i \tag{2}$$

Here, the angle θ_{i-1} represents the slope of the polynomial at the point ($x_{m_{i-1}}$,$y_{m_{i-1}}$) in the x, y baseline normalized coordinate system. The term $\tilde{y}_i$ denotes the incremental deflection in the y direction of the specific baseline point at $x_{b_i} \in [x_r, x_t]$ due to the parabolic camber morphing.

A reference coordinate system $\tilde{x}, \tilde{y}$ is defined across the morphing section, where $\tilde{y}_i$ corresponds to the deviation of a horizontal line bending into a third-order polynomial $\tilde{y}_i = k\tilde{x}_i{}^3$, representing the absolute difference between the baseline and the parabolically morphed camber. Consequently, the expression for y_{m_i} can be given as:

$$\begin{aligned} y_{m_i} &= y_{b_i} + \tilde{y}_i && (3) \\ &= y_{b_i} + k\tilde{x}_i^3 \\ &= y_{b_i} + k(x_{m_i} - x_r)^3 && (4) \end{aligned}$$

In the coordinate system $\tilde{x}, \tilde{y}$, the slope angle θ_i is established by applying an infinitesimal increment in $\tilde{y}_i$ and $\tilde{x}_i$. The underlying concept of this approach involved adjusting the infinitesimal step size ds of the baseline in the x-direction using the cosine of the polynomial's slope angle θ_i as shown in Eq. 5 and Fig. 2. By employing this approach, the stretching of the morphed camber in comparison to the baseline is avoided, ensuring that both maintain an equivalent length. The slope θ_i, which corresponds to the gradient at $(\tilde{x}_i, \tilde{y}_i)$ is progressively computed as:

$$\begin{aligned} \theta_i &= \arctan(3k\tilde{x}_i^2) && (5) \\ &= \arctan(3k(x_{mi} - x_r)^2) && (6) \end{aligned}$$

The coefficient k is therefore determined iteratively using a bisection algorithm. For each target deflection w_{TE}, a specific value of k is obtained. Two successive angles θ_i and θ_{i-1} are nearly equal in their infinitesimal difference.

Thus the coordinates x_{m_i} and y_{m_i} can be determined at every morphed point after approximating k using in the equations 1 and 2.

From x_t onwards to the aft of the airfoil, the camber line is considered to be rigid and is calculated as a linear slope. The computed morphed coordinates within this region are given by x_{m_i} and y_{m_i} :

$$\begin{aligned} x_{m_i} &= x_{m_{i-1}} + (x_{b_i} - x_{b_{i-1}})\cos(\theta_i) && (7) \\ y_{m_i} &= y_{m_{i-1}} + m_t \cdot (x_{m_i} - x_{m_{i-1}}) && (8) \end{aligned}$$

where

$$m_t = \frac{y_{m_t} - y_{m_{t-1}}}{x_{m_t} - x_{m_{t-1}}} \quad (9)$$

denotes the gradient of the linear segment that corresponds to the slope computed along the morphing interval $[x_r, x_t]$.

After determining the morphed camber for a given w_{TE}, the thickness of the baseline is applied perpendicular to the camber line along the morphing section as shown in Fig.3. Here, the half of the baseline thickness $t/2$ obtained from second step shown in Fig.1. Thus, the upper and lower surfaces of the morphed airfoil is determined using the following equations:

$$\begin{aligned} x_{u_i} &= x_{m_i} - \frac{t_i}{2}\sin(\varepsilon_i) \\ y_{u_i} &= y_{m_i} + \frac{t_i}{2}\cos(\varepsilon_i), && (10) \\ x_{l_i} &= x_{m_i} + \frac{t_i}{2}\sin(\varepsilon_i), \\ y_{l_i} &= y_{m_i} - \frac{t_i}{2}\cos(\varepsilon_i), && (11) \end{aligned}$$

where ε_i is the slope angle of the obtained morphed camber line, as suggested in [12].

The approach used to determine the morphed camber line by means of the plain flap method is analogous to the methodology applied in the FishBAC concept. In both instances, the morphed camber line was derived by transforming the aft section of the baseline configuration. However, in the case of the plain flap, a sloped line was adopted instead of employing a 3rd-order polynomial function. This method represents a rigid body rotation δ_f of the rear section about a hinge point, located at the starting of camber morphing. The coordinates of morphed section were obtained over the range $x_b \in [x_r, 1]$ as following:

$$\begin{aligned} x_{m_i} &= x_r + (x_{b_i} - x_r)\cos(\delta_f) && (12) \\ y_{m_i} &= y_{b_i} - (x_{b_i} - x_r)\sin(\delta_f) && (13) \end{aligned}$$

The angle of rotation δ_f corresponds to a given morphing deflection in chord length as a percentage of the baseline chord:

$$\delta_f = \arcsin\frac{w_{TE}}{1 - x_r}. \quad (14)$$

The surface thickness for this approach is obtained following the same approach applied for the parabolic camber morphing.

Figure 4 illustrates the difference morphed section by means of FishBAC or plain flap for the same target deflection $4\%c$ and starting for the same morphing point for

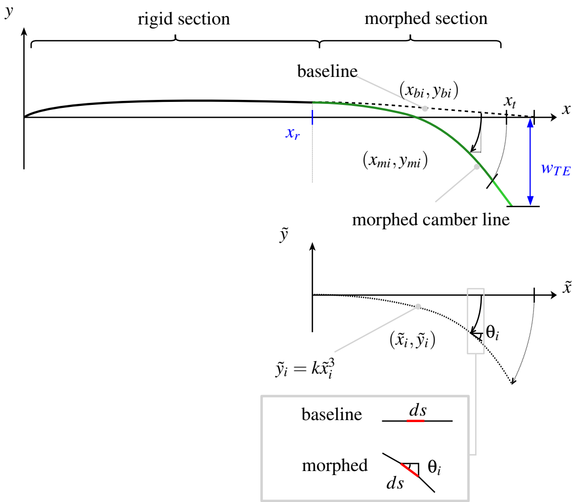

Fig. 2: Morphing of camber line based on the FishBAC concept-

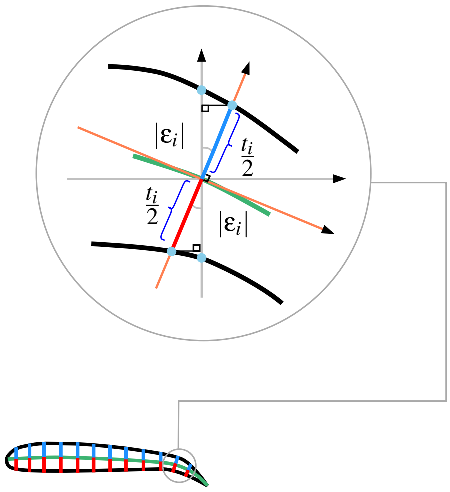

Fig. 3: Generation of the camber morphed airfoil surface.

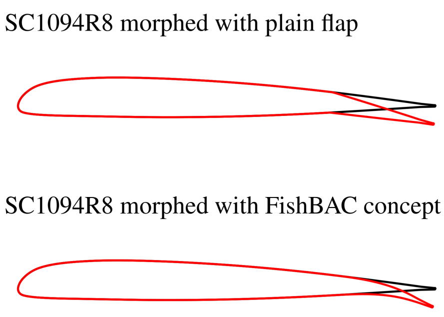

Fig. 4: Comparison between FishBAC and the plain flap in achieving an identical target deflection of $w_{TE} = 4\%c$, with the starting of camber morphing at $x_r = 75\%c$.

the baseline SC1094R8. The degree of camber morphing and the deflection of the flap were defined based on trailing-edge tip deflections as a percentage of the baseline chord. The following notation is used throughout the present work:

$$\underbrace{\text{NACA23012}}_{\text{airfoil type}},\ \underbrace{75}_{\substack{\text{beginning of camber}\\ \text{morphing } x_r \text{ in } \%c}}\ /\ \underbrace{3}_{\substack{\text{trailing edge}\\ \text{deflection } w_{TE} \text{ in } \%c}}\ ,\ \underbrace{\text{FishBAC}}_{\text{morphing concept}}$$

The resulting shapes are transferred to Pointwise to generate a 2D structured O-grid, with a radius equivalent to 50%c. A total of 200 points were allocated to both the upper and lower surfaces respectively, ensuring a distribution that effectively captures the curvature of the shape. The sizing of the initial cell is determined by the free stream velocity, calibrated such that the distance from the wall to the center of the first grid cell remains consistent with a value of one. The growth of the strucutred cells and was oriented perpendicular to the shape, is employed with a growth factor of 1.15 extending towards the boundary of the far field.

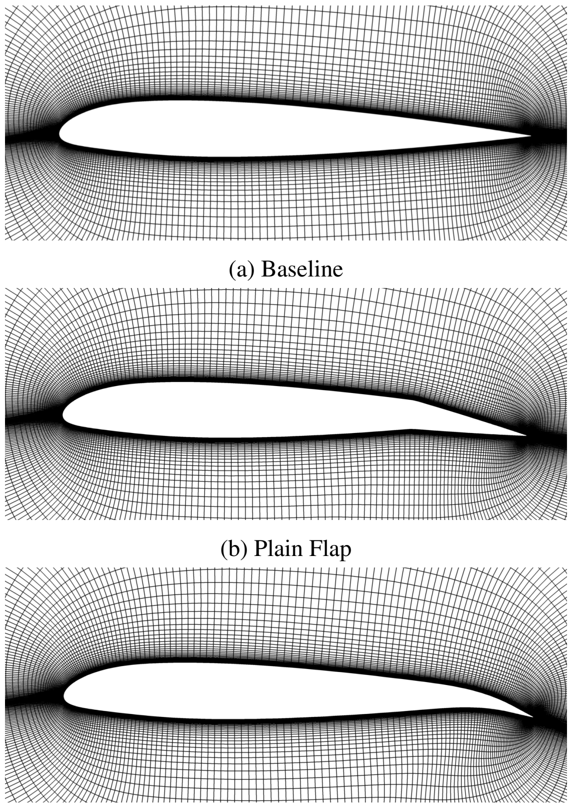

(a) Baseline

(b) Plain Flap

(c) FishBAC

Fig. 5: Illustraion of CFD grid of baseline and two representative cases for FishBAC and plain flap.

The grid generation process was automated to minimize the potential impact of grid dependence on the solutions and number of the cells used for this investigations was based on the grid convergence study for this purpose was conducted in [13].

Figure 5 shows the grid quality surrounding the airfoil and how the quality preserved for the baseline and morphed airfoils. The steady CFD investigations were conducted using the compressible solver TAU [14] across the range of angle of attack $\alpha \in [-5, \alpha_{stall}]$. In this study, the angle of attack is defined as the angle between the horizontal axis and the free stream velocity U_{∞}. Due to low computational cost and proven robustness SA-Neg model was used to solves a transport equation for kinematic eddy viscosity [13].

3 RESULTS AND DISCUSSION

This paper presents and discusses the outcomes derived from steady Computational Fluid Dynamics (CFD) investigations carried out on morphed versions of the NACA23012 and SC1094R8 airfoils. These CFD simulations were executed at a Mach number of $M = 0.4$ with a baseline chord length of 0.27 m for both airfoils.

The morphed airfoil were subjected to camber morphing deflections, ranging up to 4% of the chord length c, and starting at positions between 60% and 85% of the chord length.

The primary aim of this study was to analyze the effects of these variations on various aerodynamic parameters, including lift, drag, pitching moment, and center of pressure. A particular focus was directed towards evaluating the influence of distinct deflection levels and camber morphing starting points on the FishBAC concept. This was followed by a comprehensive comparison to the performance of the plain flap. The results of this investigation offer valuable insights into the aerodynamic behavior of the morphed airfoil adaptations and their potential implications for advanced aircraft design and performance optimization.

3.1 Validation of Numerical Setup

The numerical setup was validated using different experimental data for both the baseline airfoils. For the SC1094R8 airfoil, wind tunnel tests performed by Noonan and Dingham in 1980 at the Langley 6” by 28” Transonic Tunnel [15] were adopted as a reference to validate the drag polar. These tests were subsequently evaluated by Bousman in 2003 [16]. Figure 6a demonstrates the good agreement between the computed C_l and C_d using the numerical setup described in the methodology section.

As for the NACA23012 airfoil, the wind tunnel data compiled by Dadone in 1976 [17] served as the benchmark. Dadone’s data was extracted from a two-dimensional test conducted at the 8” by 18” blowdown tunnel at the Aircraft Research Association in Bedford, England [17]. From these experimental results, a comparison was drawn for the drag polar and the variation of the pitching moment coefficient over the angle of attack α. Figures 6b and 6c depict a comparison between the numerical data and the wind tunnel test. These figures demonstrate that aerodynamic coefficients C_l, C_d, and C_m, were well approximated using the adopted numerical setup. Thus, the validation process establishes confidence in the accuracy of the numerical setup’s results.

Variation of maximum lift coefficient

Figures 7 and 8 demonstrate a comparative analysis of the impact of morphing the baseline camber of NACA23012 and SC1094R8 on the lift-to-drag ratio C_l/C_d with respect to C_l, using both FishBAC and plain flap morphing concepts.

Regardless of the initial morphing start point or whether the morphing mechanism employed was FishBAC or plain flap, a consistent trend emerged. It was observed that an increase in deflection led to a proportional enhancement in $C_{l_{max}}$. While increasing the level of deflection, a consistent expansion of the C_l envelope towards significantly higher values was obtained, enabling the application of higher lift coefficients beyond the $C_{l_{max}}$ of the baseline configurations. For example, the most notable increase in maximum lift coefficient was observed in the highly morphed NACA23012, 85/4 FishBAC airfoil with $C_{l_{max}} = 1.9$, representing a significant 28.2% improvement over the baseline. Comparatively, the strongly morphed SC1094R8, 85/4 airfoil exhibited a 27.3% increase in $C_{l_{max}}$ over the SC1094R8 baseline. When the plain flap was applied for camber morphing, the highest C_l values were reached also with the deflection of $w_{TE} = 4\%c$. The obtained maximum lift coefficients ($C_{l_{max}}$) were comparatively lower than the values achieved using the FishBAC concept. Here, the morphed NACA23012 airfoil with the deflection of $w_{TE} = 4\%c$ achieved a maximum lift coefficient of 20.4% and the greatest $C_{l_{max}}$ obtained after morphing SC1094R8 airfoil with same deflection was 21.6%.

The FishBAC concept demonstrated an overall improvement in maximum lift compared to the plain flap, while the same morphing deflection w_{TE} was applied to both baselines NACA23012 and SC1094R8. It was consistently observed that the increase in C_l between the same deflection levels was significantly higher when the camber was morphed using FishBAC in comparison to the

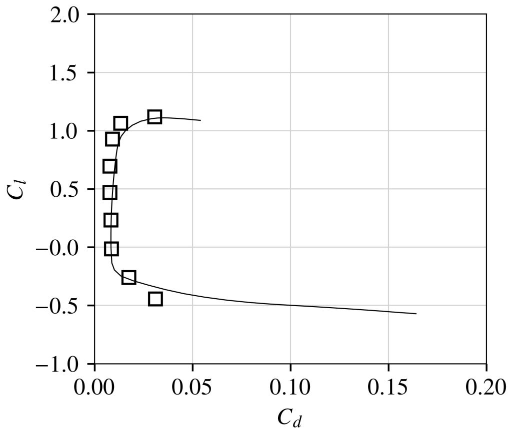

(a) Validation of the C_l over C_d for the baseline SC1094R8 airfoil by means of wind tunnel tests at $Re = 4.4E6$ and $M = 0.48$ [15, 16]

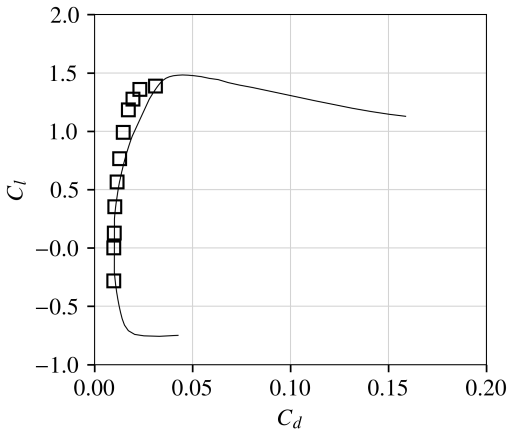

(b) Validation lift to drag of the baseline airfoil NACA23012 by means of wind tunnel tests [17] with $c = 0.127$ m, $M = 0.4$)

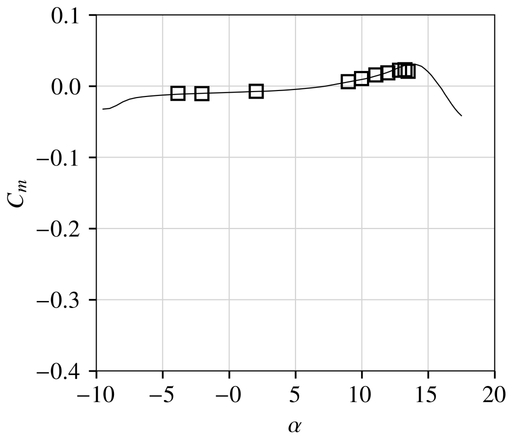

(c) Validation pitching moment of the baseline airfoil NACA23012 by means of wind tunnel tests [17] with $c = 0.127$ m, $M = 0.4$)

Fig. 6: Validation of the baseline airfoils NACA23012 and SC1094R8.

plain flap configuration. This observation can clearly seen when comparing figures 8a and 8d, or figures 7a and 7d.

Consequently, the FishBAC concept enables a significantly larger expansion of the lift range compared to the plain flap. This offers the opportunity to increase C_l while maintaining a greater safety margin to avoid stall, which is particularly critical in challenging conditions like high temperatures and high altitudes. Thus, the application of camber morphing serves as an alternative to increasing collective pitch, especially during hovering state. In scenarios, where the mean lift coefficient of the rotor can be approximated as $\bar{C_l} \approx \bar{C_L} = 6(C_T/\sigma)$, as assumed in [18], the expansion of the lift envelope allows for greater thrust generation. This can be especially relevant for heavy-lift operations, enabling the helicopter to carry a greater maximum takeoff weight. This capability can prove to be valuable, for instance, in missions involving heavy external loads, where increased lift capacity is required.

Variation of aerodynamic efficiency

The aerodynamic efficiency of a morphed airfoil can be quantified by the lift-to-drag ratio (C_l/C_d), which is evaluated with respect to changes in the lift coefficient (C_l).

Figures 7 and 8 provide valuable insights into the impact of the starting point of camber morphing on the variation. The starting camber morphing at $x_r = 65\%c$ consistently resulted in greater enhancements in C_l/C_d after surpassing a certain C_l threshold, regardless of whether the FishBAC or plain flap morphing configurations were applied. All the morphed airfoils at $x_r = 65\%c$ exhibited higher $(C_l/C_d)_{max}$ values at elevated C_l levels compared to the baselines. The $(C_l/C_d)_{max}$ values achieved with the FishBAC approach were slightly larger in comparison to the plain flap configuration. Additionally, FishBAC consistently generated C_l/C_d values exceeding the baseline $(C_l/C_d)_{max}$ over a wider range of C_l when compared to the plain flap configuration.

Furthermore, the closer the starting of camber morphing was to the trailing edge, the enhancement of C_l/C_d combined with a greater expansion of the lift capability. For instance, when maintaining a constant C_l/C_d greater than the baseline $(C_l/C_d)_{max}$, the increase in C_l exhibited a more gradual progression and a greater difference between two consecutive deflections. However, this is only valid for the low and medium morphed shaped, since the airfoils with the greatest deflection ($w_{TE} = 4\%c$) and starting morphing from $x_r = 85\%c$, induced notably lower C_l/C_d values in comparison to the baselines across the entire range of considered C_l. This suggests that even though

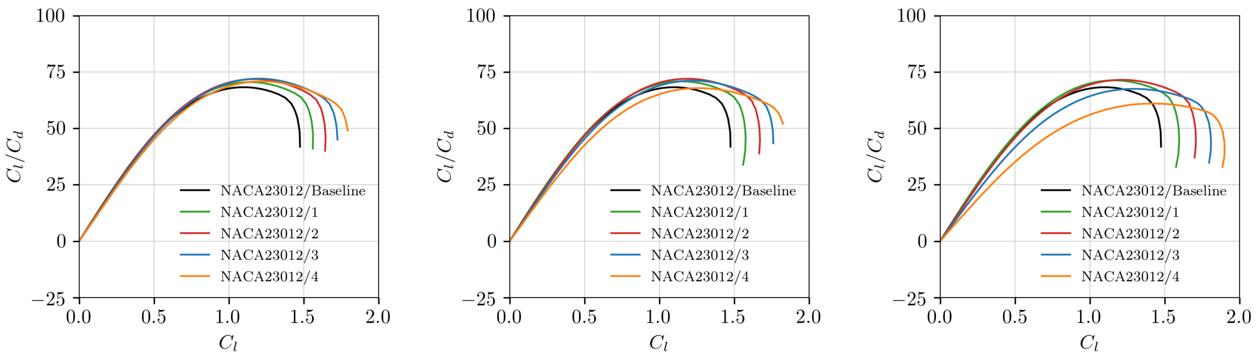

(a) NACA23012 FishBAC $x_r = 65\%c$ (b) NACA23012 FishBAC $x_r = 75\%c$ (c) NACA23012 FishBAC $x_r = 85\%c$

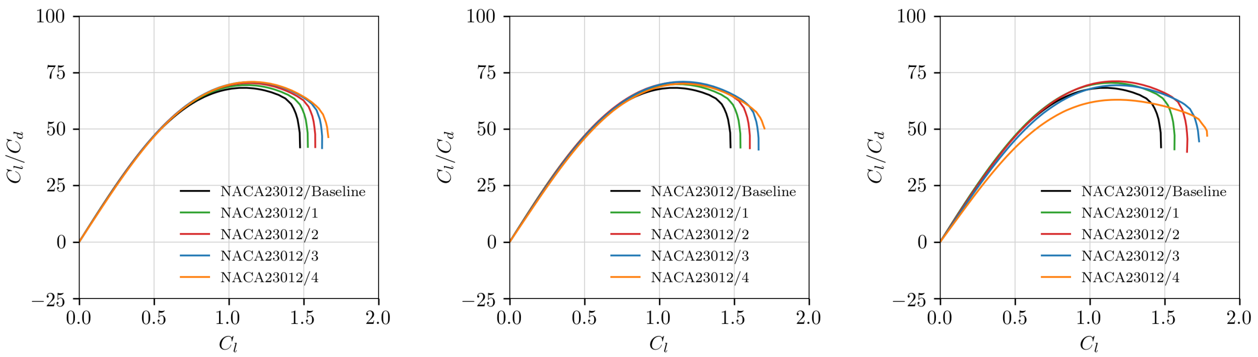

(d) NACA23012 plain flap $x_r = 65\%c$ (e) NACA23012 plain flap $x_r = 75\%c$ (f) NACA23012 plain flap $x_r = 85\%c$

Fig. 7: Comparison of the steady C_l/C_d between the FishBAC and plain flap at different deflection angles, with various morphing starting points for the baseline airfoil NACA23012.

airfoils with the greatest deflection at $x_r = 85\%c$ could achieve higher C_l values, these morphed airfoils induced substantial increase in drag compared to the baseline and cases with low morphing deflection.

It was consistently observed that morphing both baseline airfoils with $2\%c$ and $3\%c$ (medium deflections) led to improvements in C_l/C_d ratio compared to the baselines, regardless of the starting point of camber morphing. This improvement was extended over significantly large C_l values, as the camber morphing started further towards the trailing edge. As a result, applying moderate deflections enables the design of blade sections with notably enhanced aerodynamic efficiency at C_l values near the maximum baseline $C_{l_{max}}$, with no additional drag penalty. This improvement is more pronounced with FishBAC compared to the plain flap configurations. Assuming a constant rotor solidity, this enhancement can lead to improved rotor efficiency during hover, resulting in a higher figure of merit. Alternatively, employing high-lift morphed airfoil sections can facilitate lower tip speeds while maintaining the same solidity. This can be achieved by generating higher mean lift values without inducing a drag increase or approaching the stall limits.

Figures 9 and 10 depict how the $(C_l/C_d)_{max}$ varied depending on the level of camber morphing and the starting point of morphing. This presentation illustrates that with greater camber morphing applied towards the trailing edge, a lower level of deflection is required to improve $(C_l/C_d)_{max}$. The greatest improvement in $(C_l/C_d)_{max}$ was achieved with a moderate levels of camber morphing and a starting morphing point x_r further towards the leading edge. In terms of $(C_l/C_d)_{max}$, the FishBAC concept demonstrated superior performance compared to the plain flap. This is particularly evident when considering the SC1094R8 airfoil. This observation is further supported by the data presented in Table 1, which summarizes the highest $(C_l/C_d)_{max}$ values achieved for the considered morphing deflections using FishBAC. The table shows also the obtained improvement in comparison to the baseline airfoils and the plain flap configurations.

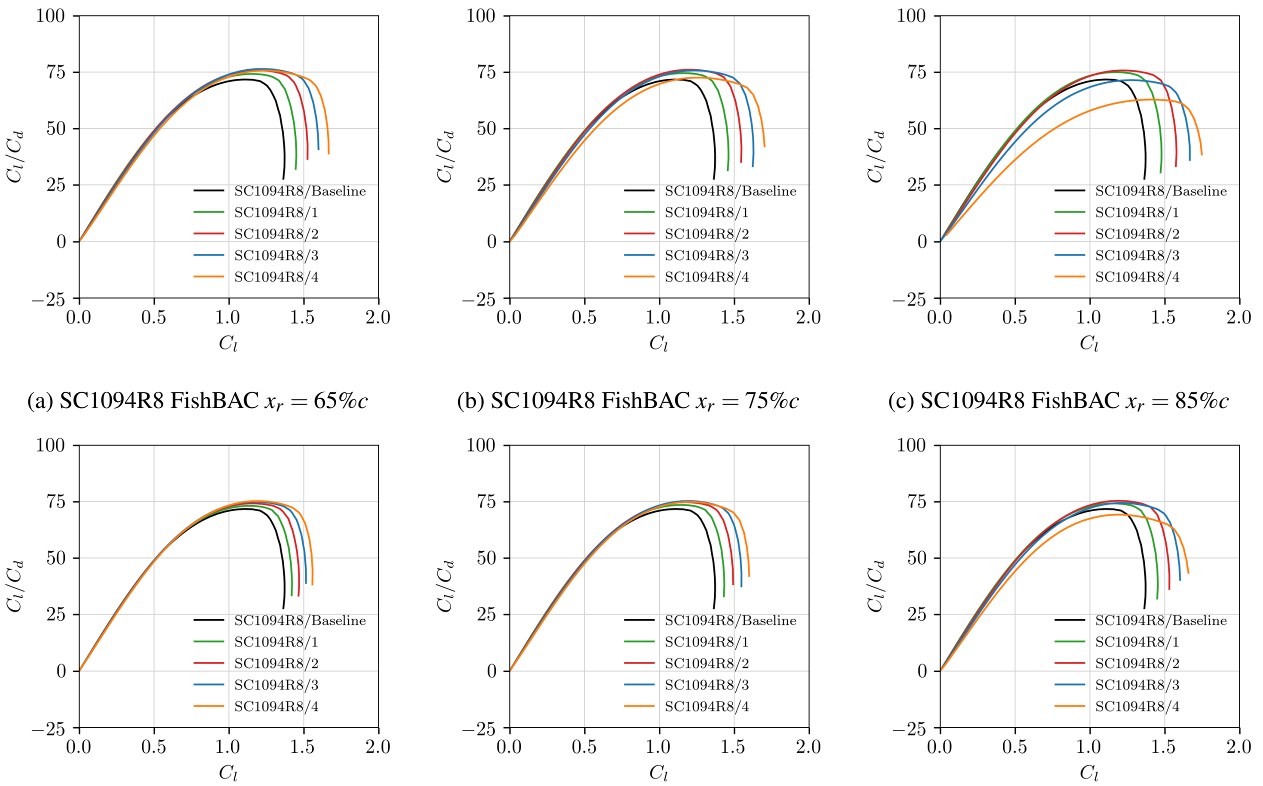

(a) SC1094R8 FishBAC $x_r = 65\%c$ (b) SC1094R8 FishBAC $x_r = 75\%c$ (c) SC1094R8 FishBAC $x_r = 85\%c$

(d) SC1094R8 plain flap $x_r = 65\%c$ (e) SC1094R8 plain flap $x_r = 75\%c$ (f) SC1094R8 plain flap $x_r = 85\%c$

Fig. 8: Comparison of the steady C_l/C_d between the FishBAC and plain flap at different deflection angles, with various morphing starting points for the baseline airfoil SC1094R8.

Airfoil	$(C_l/C_d)_{\max}$	Improvement over the baseline [%]	Improvement over the plain flap [%]
NACA23012, 60 / 3, FishBAC	72.2	5.7	2.1
NACA23012, 65 / 3, FishBAC	72.1	5.6	1.8
NACA23012, 70 / 2, FishBAC	71.9	5.3	1.9
NACA23012, 75 / 2, FishBAC	72.0	5.4	1.7
NACA23012, 80 / 2, FishBAC	71.9	5.3	1.3
SC1094R8, 60 / 3, FishBAC	76.5	6.7	2.4
SC1094R8, 65 / 3, FishBAC	76.4	6.6	2.0
SC1094R8, 70 / 3, FishBAC	76.2	6.3	1.4
SC1094R8, 75 / 2, FishBAC	76.1	6.1	1.8
SC1094R8, 80 / 2, FishBAC	76.1	6.1	1.4

Table 1: The greatest aerodynamic efficiency, denoted as $(C_l/C_d)_{\max}$ achieved through camber morphing using the FishBAC concept and in comparison to the baseline airfoil as well as the corresponding plain flap variant.

Variation of pitching moment

The evaluation of the pitching moment coefficient (C_m) was conducted at the quarter chord location with respect to C_l for each morphed airfoil, and this was compared to the respective baseline airfoil. This analysis aimed to understand the influence of camber morphing using FishBAC and plain flap on the variation of pitching moment.

Figures 12 and 13 illustrate the changes in C_m values for the baselines NACA23012 and SC1094R8 after morphing the camber through the FishBAC and plain flap methods.

As the deflection level increased, the C_m-curves consistently were shifted towards higher C_l-values and reached lower negative C_m-values, indicating a rise in nose-down pitching moments.

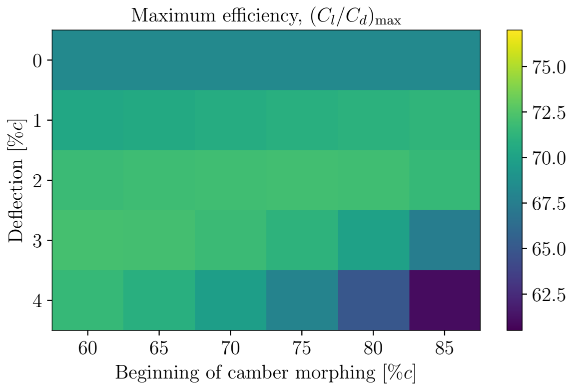

(a) NACA23012 morphed with FishBAC.

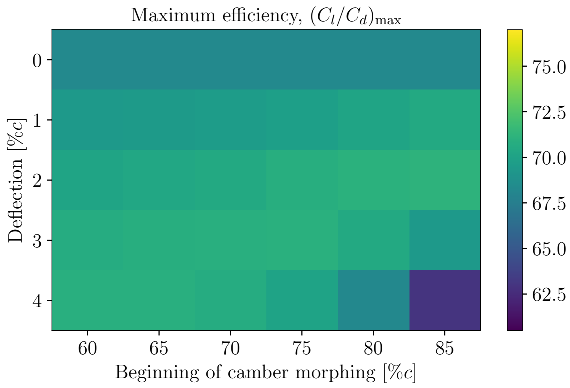

(b) NACA23012 morphed with plain flap.

Fig. 9: Comparison of the steady $(C_l/C_d)_{max}$ between the FishBAC and plain flap at different deflection angles, with various morphing starting points for the baseline airfoil NACA23012.

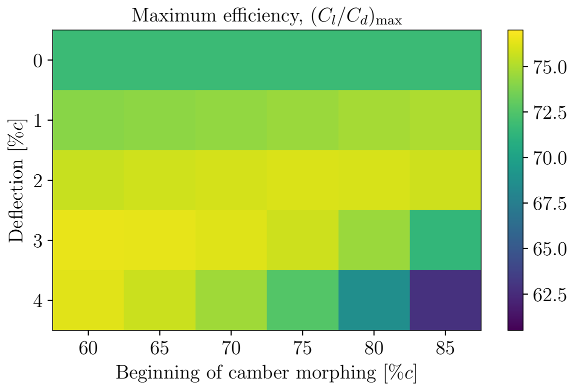

(a) SC1094R8 morphed with FishBAC.

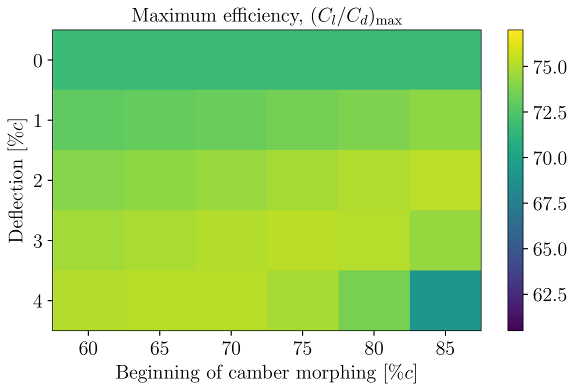

(b) SC1094R8 morphed with plain flap.

Fig. 10: Comparison of the steady $(C_l/C_d)_{max}$ between the FishBAC and plain flap at different deflection angles and with different starting point for morphing for the baseline airfoils SC1094R8.

Shifting the starting point of camber morphing towards the trailing edge led to a consistent shift of the C_m-curve towards higher C_l-values and more negative C_m-values.

The FishBAC camber morphed airfoils generally exhibited larger $|C_m|$-values compared to the corresponding plain flap versions. This became more significant as the deflection level increased. This effect was most notable when camber morphing commenced at $x_r = 65\%c$. Specifically, the C_m curves resulting from various deflections using plain flap exhibited a closer clustering, whereas the C_m curves obtained after morphing the baseline with FishBAC exhibited more distinct variations.

Additionally, it was also observed that with an increase in deflection, the C_m variation over C_l became more nonlinear within the range of $[0, C_{l_{max}}]$. This implies that the sensitivity to pitching moment increases in response to changes in lift. This aspect should be considered in the design of helicopter control and stability systems, particularly during forward flight where lift changes along the azimuth at specific radial positions. Moreover, the increased magnitudes of C_m could lead to increased root stress loads at the blade root and control linkages, as noted in [19, 20].

The morphing of camber results in increased pressure differentials between the upper and lower surfaces of the airfoil, as shown in [13]. This led to higher values of the pitch moment coefficient $|C_m|$ compared to the baseline configuration. Figure 16 illustrates how the pressures pattern on the baseline airfoil NACA23012 changed while the FishBAC and plain flap were applied from $x_r = 75\%c$. There was an amplification of the suction peak compared to the baseline, coupled with an observed increase in the pressure difference between the lower and upper surfaces, as shown in Fig. 16.

The difference in the pressure distribution between the FishBAC and plain flap configurations was most pronounced along the morphing section, where the suction force increased followed by a sudden drop. In contrast, FishBAC configuration resulted in a smoother pressure distribution over the morphing section.

As the degree of deflection increased to $w_{TE} = 4\%c$, the sharp curvature of the plain flap caused a pronounced change in pressure distribution, resulting in a more significant knick and the formation of a reverse flow region occurring farther upstream compared to the FishBAC configuration, as shown in Fig.11. This factor should be taking in account when selecting between the FishBAC or plain flap configurations for maximizing lift generation. Moreover, it was observed that starting point of camber morphing x_r affected the size and extension of the reverse flow region. Consequently, this can impact the aerodynamic efficiency expressed as C_l/C_d.

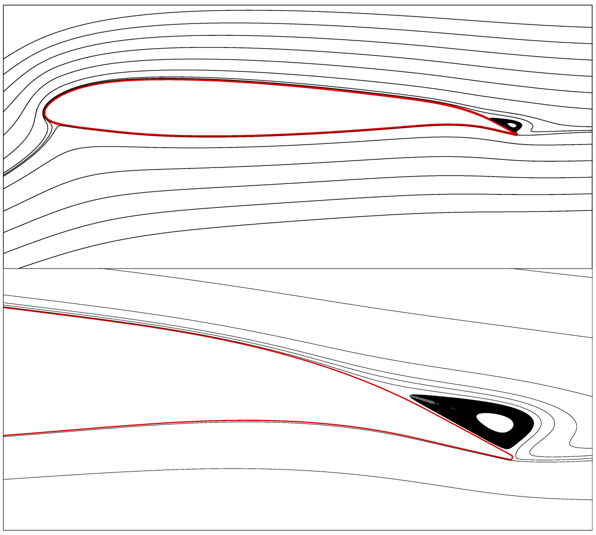

(a) NACA23012 morphed with FishBAC with $w_{TE} = 4\%c$ and $x_r = 75\%c$.

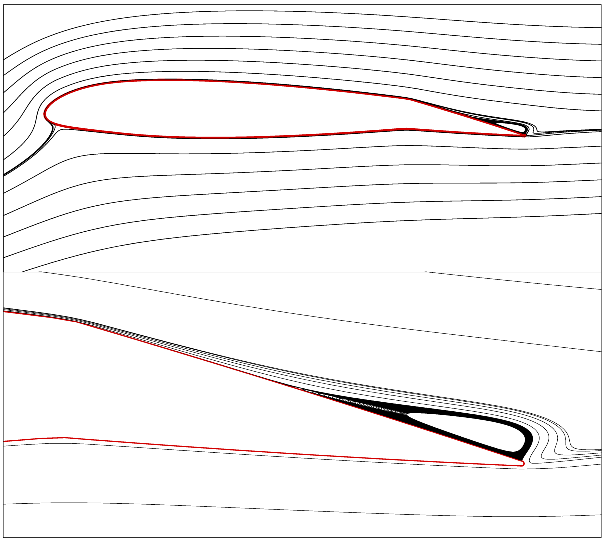

(b) NACA23012 morphed with plain flap with $w_{TE} = 4\%c$ and $x_r = 75\%c$.

Fig. 11: Comparison of the reverse flow region induced by camber morphing using FishBAC and plain flap.

The impact of airfoil morphing on the location of the center of pressure x_{cp}, which represents the point where the total normal and axial forces are acting, is computed as suggested in [18] as:

$$x_{cp} = \frac{1}{4} - \frac{C_{m1/4}}{C_n}, \text{ where } C_n = C_l cos(\alpha) + C_d sin(\alpha) \quad (15)$$

Figures 14 and 15 illustrate that the center of pressure for the baseline airfoils was predominantly positioned around the quarter chord ($x = 25\%c$) and remained relatively unchanged regardless of lift variations. In contrast, as the level of morphing was increased, the x_{cp} location shifts towards the trailing edge for the same low C_l values. With an increase in the targeted lift, x_{cp} also moved closer to the quarter chord, which corresponds to the aerodynamic center. The displacement of the center of pressure was less prominent when initiating morphing at $x = 65\%c$ using the plain flap configuration, while it became most significant with the starting point of camber morphing at $x_r = 85\%c$ for both configurations. Additionally, it was noted that the center of pressure's location is highly sensitive to the starting point of camber morphing when employing the plain flap approach.

This shift of the center of pressure, which is defined as the position where lift and drag forces act, directly affected the pitch moment. This shift amplified the downward pitch moment as the center of pressure migrated towards the trailing edge. The considerable displacement of the center of pressure had significant implications for the analysis of longitudinal stability in aircraft or helicopters [21]. This aspect became particularly critical when considering variations in the angle of attack (lift) and the dynamic morphing of the airfoil.

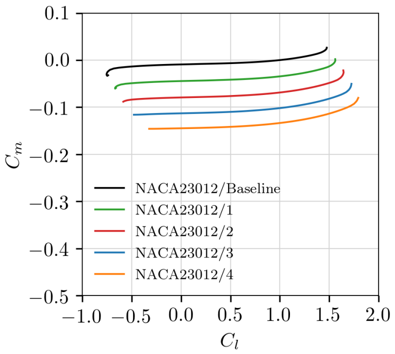

(a) NACA23012 FishBAC $x_r = 65\%c$

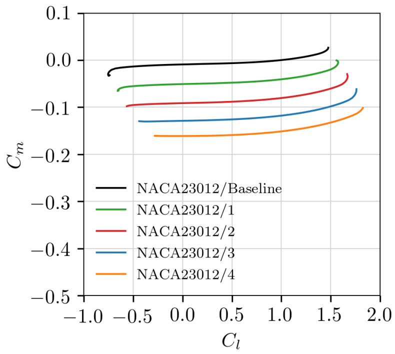

(b) NACA23012 FishBAC $x_r = 75\%c$

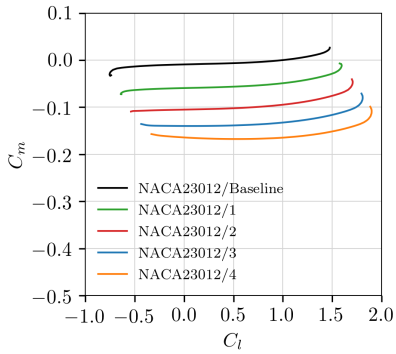

(c) NACA23012 FishBAC $x_r = 85\%c$

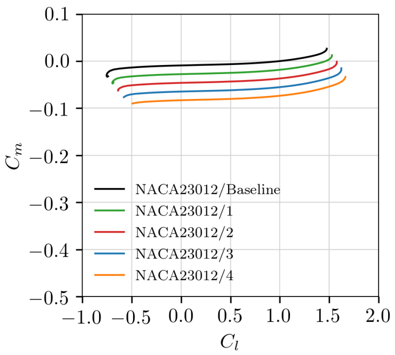

(d) NACA23012 plain flap $x_r = 65\%c$

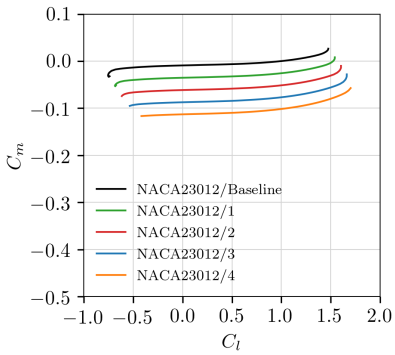

(e) NACA23012 plain flap $x_r = 75\%c$

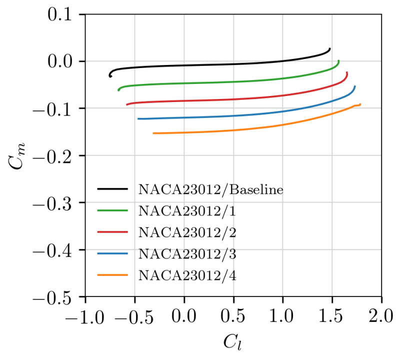

(f) NACA23012 plain flap $x_r = 85\%c$

Fig. 12: Comparison of the steady pitching moment C_m between the FishBAC and plain flap at different deflection angles, with various morphing starting points for the baseline airfoil NACA23012.

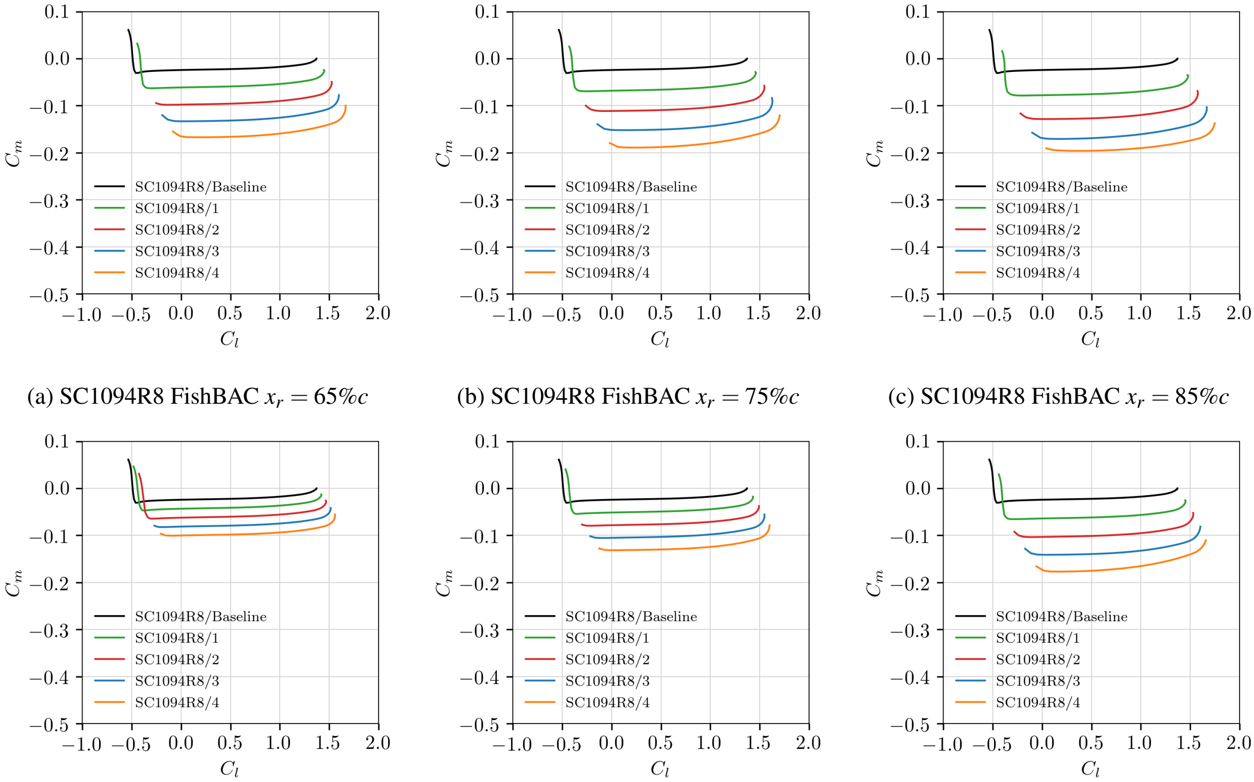

(a) SC1094R8 FishBAC $x_r = 65\%c$

(b) SC1094R8 FishBAC $x_r = 75\%c$

(c) SC1094R8 FishBAC $x_r = 85\%c$

(d) SC1094R8 plain flap $x_r = 65\%c$

(e) SC1094R8 plain flap $x_r = 75\%c$

(f) SC1094R8 plain flap $x_r = 85\%c$

Fig. 13: Comparison of the steady pitching moment C_m between the FishBAC and plain flap at different deflection angles, with various morphing starting points for the baseline airfoil SC1094R8.

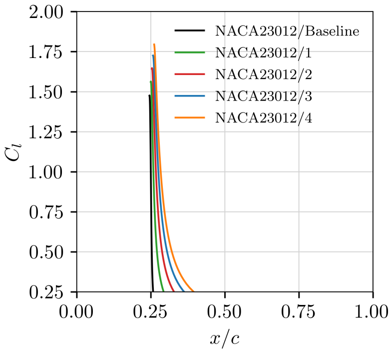

(a) NACA23012 FishBAC $x_r = 65\%c$

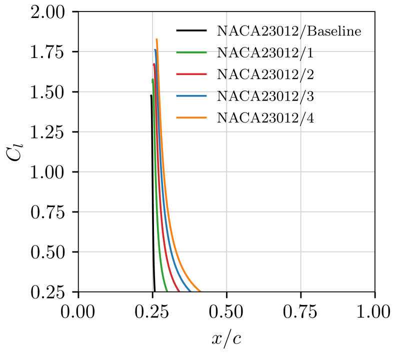

(b) NACA23012 FishBAC $x_r = 75\%c$

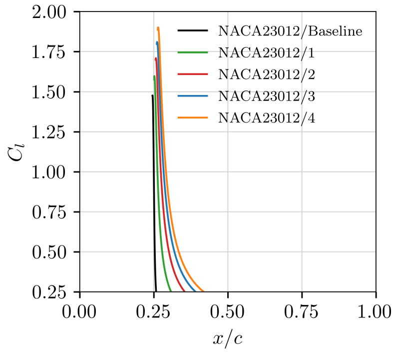

(c) NACA23012 FishBAC $x_r = 85\%c$

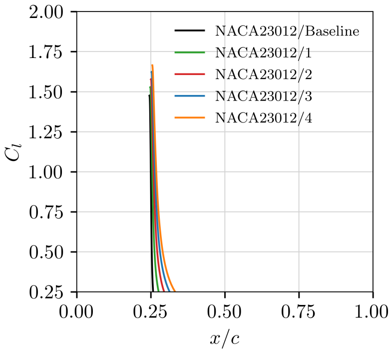

(d) NACA23012 plain flap $x_r = 65\%c$

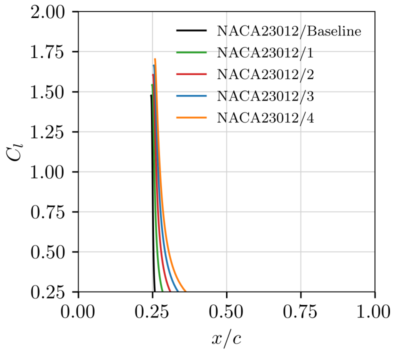

(e) NACA23012 plain flap $x_r = 75\%c$

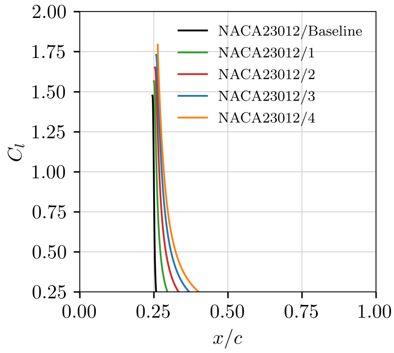

(f) NACA23012 plain flap $x_r = 85\%c$

Fig. 14: Comparison of the centre of pressure between the FishBAC and plain flap at various deflection angles and morphing starting points for the baseline NACA23012 airfoil.

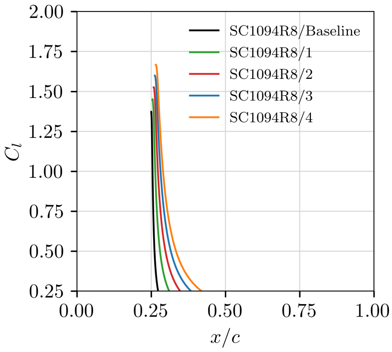

(a) SC1094R8 FishBAC $x_r = 65\%c$

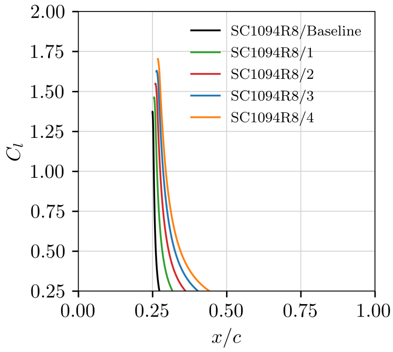

(b) SC1094R8 FishBAC $x_r = 75\%c$

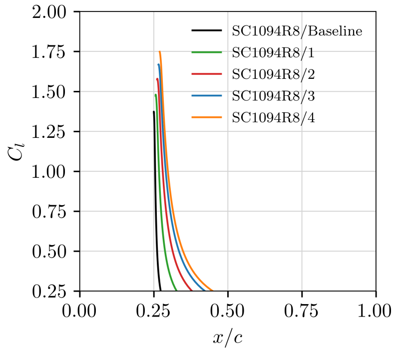

(c) SC1094R8 FishBAC $x_r = 85\%c$

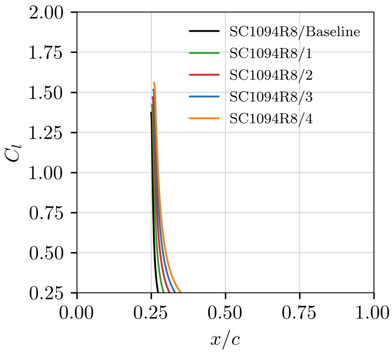

(d) SC1094R8 plain flap $x_r = 65\%c$

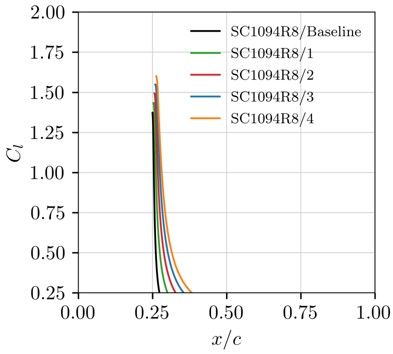

(e) SC1094R8 plain flap $x_r = 75\%c$

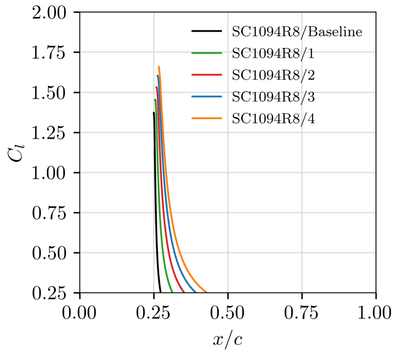

(f) SC1094R8 plain flap $x_r = 85\%c$

Fig. 15: Comparison of the centre of pressure between the FishBAC and plain flap at various deflection angles and morphing starting points for the baseline SC1094R8 airfoil.

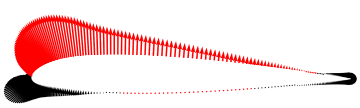

(a) NACA23012 Baseline,$\alpha = 4°$, $w_{TE} = 0\%c$

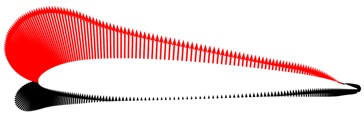

(b) NACA23012 FishBAC, $\alpha = 4°$, $w_{TE} = 2\%c$

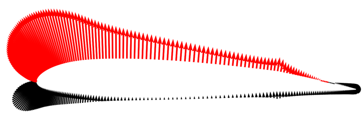

(c) NACA23012 plain flap, $\alpha = 4°$, $w_{TE} = 2\%c$

Fig. 16: Pressure Pattern Comparison: Comparison of FishBAC and plain flaps at deflection $w_{TE} = 2\%c$ with a starting deflection at $x_r/c = 75\%c$ for the baseline NACA23012 airfoil.

4 CONCLUSION AND OUTLOOK

In the present study, the steady aerodynamic characteristics of camber morphed NACA23012 and SC1094R8 airfoils were investigated. Geometrical representations of the FishBAC concept and the plain flap have been developed featuring a transformation of camber line coordinates. These transformations were based on a 3rd order polynomial function and a sloped line respectively. Trailing edge deflections of up to $4\%c$ and starting of camber morphing from 60 to $85\,\%c$ were considered. The aerodynamic characteristics of the FishBAC configurations were evaluated and compared to the plain flap as well as to the corresponding baselines. The CFD simulations were performed at a free stream Mach number of $M = 0.4$ and angles of attack $\alpha \in [-5, \alpha_{max}]$. The present investigation yielded the following specific conclusions:

- As the degree of deflection was increased, a consistent expansion of the C_l envelope to significantly higher values was obtained, allowing the application of higher lift coefficients beyond the $C_{l_{max}}$ of the baseline configurations. The most notable increase in the maximum lift coefficient was obtained in the highly morphed NACA23012, 85/4 FishBAC airfoil with $C_{l_{max}} = 1.9$, representing a significant 28.2% improvement over the baseline. In comparison, the heavily morphed SC1094R8, 85/4 airfoil showed a 27.3% increase in $C_{l_{max}}$ over the SC1094R8 baseline.

- In cases where the plain flap was employed for camber morphing, the most elevated C_l values were attained also through a deflection of $w_{TE} = 4\%c$. However, the achieved maximum lift coefficients were lower compared to the FishBAC concept. Specifically, for the NACA23012 airfoil undergoing camber morphing with a deflection of $w_{TE} = 4\%c$, the maximum lift coefficient was 20.4%, while for the SC1094R8 airfoil with the same deflection, the highest $C_{l_{max}}$ achieved was 21.6%. This emphasizes the distinct effects and outcomes caused by different morphing techniques.

- The airfoil variants that yielded the highest maximum efficiency ranged from large deflections and forward starting of camber morphing up to moderate deflections starting closer to the trailing edge. In this area, the FishBAC variants generally obtained higher $(C_l/C_d)_{\max}$ values compared to the plain flap. For instance, the airfoils NACA23012, 60 / 3, FishBAC and SC1094 R8, 60 / 3, FishBAC achieved improvements in $(C_l/C_d)_{\max}$ of 5.7 % and 6.7 % over the baseline, while outperforming the corresponding plain flap variants by 2.1 % and 2.4 % respectively. However, towards large deflections combined with a beginning of it near the trailing edge, the maximum efficiency of both camber morphing concepts declined significantly. Here, the plain flap yielded higher $(C_l/C_d)_{\max}$ values than the FishBAC concept.

- The FishBAC camber morphed airfoils generally demonstrated greater absolute values of C_m in comparison to the corresponding plain flap variants. This trend became increasingly pronounced as the deflection level increased. The C_m values obtained from different deflection angles using plain flap showed a tighter clustering, whilst the curves attained after morphing the baseline with FishBAC exhibited more noticeable variations. This should be taken into account when designing control and stability systems for helicopters, especially in forward flight where lift changes along the azimuth at certain radial positions. Furthermore, the increased amounts of C_m could lead to increased root stresses at the blade root and pitch links.

- There was an increase in the suction peak compared to the baseline, which was accompanied by an observed rise in the pressure difference between the upper and lower surfaces. The difference in pressure distribution between the FishBAC and the plain flap configurations was primarily noticeable in the morphing section. The plain flap configuration indicated a suction force increase at the starting of the morphing section, followed by an abrupt decrease caused by the sharp curvature. In contrast, the FishBAC configuration demonstrated a smoother pressure distribution across the corresponding morphing area. The notable kink formation caused by plain flap induced a reverse flow region which was extended from the trailing edge to further upstream compared to the FishBAC configuration.

- When raising the deflection level or moving the starting of camber morphing further aft, the center of pressure was shifted downstream. This trend was caused by the increased nose down pitching moments. Furthermore, airfoil variants based on the FishBAC concept generally exhibited higher x_{cp} values compared to the plain flap.

- The movement of the center of pressure was pronounced when morphing commenced at $x_r = 65\%c$ using the plain flap configuration, whereas it became most pronounced when the initiation of morphing occurred at $x_r = 85\%c$ for both configurations. Additionally, the position of the center of pressure exhibited sensitivity to the point of starting camber morphing when the plain flap was applied.

In conclusion, the present results indicate that the FishBAC concept allows for significant improvements in lift and efficiency over the baseline and the plain flap. However, whether the specific variants that yielded these improvements would be preferable to the baseline or the plain flap depends on the tolerable pitching moments.

The obtained data may be used as the basis for complete rotor comprehensive analyses featuring active rotor concepts operating at various actuation frequencies. Aerodynamic effects that were not considered in the present static investigation, such as dynamic stall, are a subject for further research. Additionally, an investigation of camber morphed rotor airfoils at higher Mach numbers could provide insight on how a variation of the free stream velocity would affect the previously drawn conclusions.

5 ACKNOWLEDGMENT

This research was initiated under the SABRE project and initially funded by the European Union's Horizon 2020 research and innovation program through grant agreement number 723491. Subsequently, it was further supported through the LuFo VI-2 program, sponsored by the German Federal Ministry for Economic Affairs and Climate Action under grant number 20E2108A for the ARCTIS project.

Supported by:

Federal Ministry for Economic Affairs and Climate Action

6 COPYRIGHT STATEMENT

7 REFERENCES

[1]Bousman, W. G., "Airfoil design and rotorcraft performance," 2002.

[2]Rauleder, J., van der Wall, B. G., Abdelmoula, A., Komp, D., Kumar, S., Ondra, V., Titurus, B., and Woods, B. K. S., "Aerodynamic Performance of Morphing Blades and Rotor Systems," *AHS International 74th Annual Forum & Technology Display*, , No. May, 2018.

[3]Woods, B. K. S., Bilgen, O., and Friswell, M. I., "Wind tunnel testing of the fish bone active camber morphing concept," *Journal of Intelligent Material Systems and Structures*, 2014.

[4]Hunsaker, D. F., Reid, J., and Moorthamers, B., "Geometry and Aerodynamic Performance of Parabolic Trailing-Edge Flaps," 2018.

[5]Woods, B. K. and Friswell, M. I., "Multi-objective geometry optimization of the Fish Bone Active Camber morphing airfoil," *Journal of Intelligent Material Systems and Structures*, Vol. 27, No. 6, 2016, pp. 808–819.

[6]Komp, D., Kumar, S., Abdelmoula, A., Hajek, M., and Rauleder, J., "Investigation of active rotor design and control for performance improvement," *Vertical Flight Society 75th Annual Forum*, 2019.

[7]Komp, D., Kumar, S., Hajek, M., and Rauleder, J., "Effect of active camber morphing on rotor performance and control loads," *Aerospace Science and Technology*, Vol. 108, 2021, pp. 106311.

[8]Komp, D., Hajek, M., and Rauleder, J., "Rotor Performance Enhancements with Spanwise Varying Active Camber Morphing," *AIAA Scitech 2021 Forum*, 2021, p. 0200.

[9]Johnson, W., *Rotorcraft Aeromechanics*, 2013.

[10]Totah, J., "A critical assessment of UH-60 main rotor blade airfoil data," 2013.

[11]Woods, B. K. S. and Friswell, M. I., "Preliminary Investigation of a Fishbone Active Camber Concept," *ASME 2012 Conference on Smart Materials, Adaptive Structures and Intelligent Systems*, 2012.

[12]Abbott, I. H., *Theory of Wing Sections*, 1959.

[13]Abdelmoula, A. and Rauleder, J., "Aerodynamic Performance of Morphed Camber Rotor Airfoils," 2019.

[14]Deutsches Zentrum für Luft- und Raumfahrt e.V, "Technical Documentation of the DLR TAU-Code Release 2018.1.0," Tech. rep., 2018.

[15]Noonan, K. W. and Dingham, G. J., "Aerodynamic characteristics of three helicopter rotor airfoil sections at Reynolds number from model scale to full scale at Mach numbers from 0.35 to 0.90. [conducted in Langley 6 by 28 inch transonic tunnel]," Tech. rep., 1980.

[16]Bousman, W. G., "Aerodynamic Characteristics of SC1095 and SC1094 R8 Airfoils," 2003.

[17]Dadone, L. U., "Design and Analytical Study of a Rotor Airfoil," Tech. rep., NASA, 1978.

[18]Leishman, G., *Principles of Helicopter Aerodynamics*, 2006.

[19]Jain, R., Yeo, H., and Chopra, I., "Examination of rotor loads due to on-blade active controls for performance enhancement," *Journal of aircraft*, Vol. 47, No. 6, 2010, pp. 2049–2066.

[20]Thibert, J.-J. and Pouradier, J., *Design and test of an helicopter rotor blade with evolutive profile*, Office National d'Études et de Recherches Aérospatiales, 1980.

[21]Young, A., "Aerodynamics. By LJ CLANCY. Pitman, 1975. 610 pp.£ 10.00." *Journal of Fluid Mechanics*, Vol. 77, No. 3, 1976, pp. 623–624.